Journal of Electronic Materials
https://doi.org/10.1007/s11664-025-12274-y

ORIGINAL RESEARCH ARTICLE

Enhancing Drain Current in Nano-carbon Transistors: Simulation and Modeling with $LaAlO_3$ Dielectric Under NH_3 Exposure

Hana Laouar[1,2] · Saadeddine Khemissi[1,2] · Linda Aissani[1,3] · Ahcen Keziz[4] · Taha Abdel Mohaymen Taha[5]

Received: 26 April 2025 / Accepted: 21 July 2025
© The Minerals, Metals & Materials Society 2025

Abstract
We have developed and analyzed an analytical model of a double-gate graphene nanoribbon field-effect transistor (GNR-FET), which is subsequently evaluated through numerical simulations, to investigate its potential as an ammonia (NH_3) gas sensor. Using lanthanum aluminate ($LaAlO_3$), known for its high dielectric constant ($K = 30$), serves as a gate dielectric in the configuration of GNRFET gas sensors to minimize short-channel effects and leakage current. The study investigates the static characteristics of the device both in the presence and absence of ammonia gas, providing insights into its potential for gas detection. Following the determination of the device structure, the drain current is calculated as a function of gate and drain bias voltages. The general current equation is enhanced by incorporating expressions that account for the influence of NH_3 gas and temperature variations. These mathematical formulations are then utilized to develop a comprehensive simulation program. The simulation is conducted on GNRFET devices with gate lengths ranging from 100 nm to 300 nm, and NH_3 gas concentrations from 300 ppm to 500 ppm. The simulation results provide insight into how various parameters affect the performance of GNRFETs. Our findings demonstrate that GNRFETs exhibit significant potential as high-quality NH_3 gas sensors, highlighting their applicability in environmental monitoring and sensor technology.

Keywords GNRFET · *I*–*V* characteristics · graphene · $LaAlO_3$ · NH_3 gas

Introduction

Graphene, a monolayer of carbon atoms arranged in a hexagonal lattice, is heralded as a groundbreaking material in the realm of electronics and optoelectronics. Its unique properties stem from its two-dimensional (2D) structure, which not only contributes to its strength but also significantly influences its electrical characteristics. One of the most remarkable features of graphene is its exceptional electrical conductivity, attributed to the presence of π-bonds that allow for high electron mobility. This means that electrons can move through graphene more freely than they can in conventional semiconductor materials, resulting in superior performance in electronic applications. In the context of field-effect transistors (FETs), graphene serves as an ideal conductive channel. Unlike traditional semiconductor materials such as silicon, which can be limited by their intrinsic charge carrier mobility, graphene boasts charge mobility values that can exceed 20,000 $cm^2/V\ s$ under optimal conditions.[1–3] This high mobility not only enables quicker response times in electronic circuits but also supports the development of high-frequency and high-speed devices. Moreover, graphene's physical properties provide additional advantages for FETs.[4] Additionally, graphene exhibits a linear energy band structure near the Dirac point, which allows for a high ON/OFF current ratio, making it suitable for analog and digital applications alike. Graphene is also

✉ Ahcen Keziz
ahcen.keziz@univ-msila.dz

✉ Taha Abdel Mohaymen Taha
Correspondencetaha.hemida@yahoo.com

1 Matter Sciences Department, Institute of ST Abbes Laghrour University Khenchela, Khenchela, Algeria

2 ISMA Laboratory of Engineering and Advanced Materials Science, Abbes Laghrour University, 40000 Khenchela, Algeria

3 Active Components and Materials Laboratory, Larbi Ben M'Hidi University, 40000 Oum El Bouaghi, Algeria

4 Physics and Chemistry of Materials Laboratory, Department of Physics, University Pole, 28000 M'sila, Algeria

5 Physics and Engineering Mathematics Department, Faculty of Electronic Engineering, Menoufia University, Menouf 32952, Egypt

noteworthy for its thermal conductivity, which is among the highest of any known material. This characteristic is advantageous in managing heat generation in electronic devices, further contributing to their reliability and performance.[5] The combination of high charge mobility, excellent thermal properties, and a versatile platform for integration with other materials positions graphene as a frontrunner in the next generation of electronic and optoelectronic devices.[6,7]

Due to its nearly negligible effective mass, graphene exhibits strong carrier mobility, significant current density, high saturation velocity, and high cut-off frequency, which are all measured in units of 2.75×10^5 cm^2/V^{-s}, 2×10^8 A/cm^2, 5.5×10^7 cm/s, and 100 GHz, respectively.[8] This substance has a zero-bandgap, although, when it is at the nanometric scale, lateral quantum confinement causes a bandgap to open up. Graphene nanoribbons (GNRs), which are thin graphene strips with a width of less than 100 nm, have limited energy.[9,10] The outstanding current carrying capacity of GNRs is higher than 10^8 A/cm^2 for widths as small as 16 nm. The breakdown voltage is also predicted to be 2.5 V for GNRs that are 22 nm in width.[11–14] GNRs are utilized as channel material in transistors, and graphene nanoribbon field-effect transistors (GNRFETs) are GNR-based transistors that are experimentally and conceptually viable alternatives to complementary metal–oxide–semiconductor (CMOS) devices.[15]

Two-dimensional (2D) materials have attracted significant attention for gas-sensing applications due to their atomic thickness, high surface-to-volume ratio, and tunable electronic properties, which enable enhanced sensitivity and fast response times at room temperature,[16,17] encompassing graphene, black phosphorus, transition metal chalcogenides, and layered metal oxides.[18] Transition metal dichalcogenides such as MoS_2 and WS_2 have demonstrated remarkable gas-sensing performance, especially when functionalized with catalytic nanoparticles or combined in heterostructures that improve charge transfer and selectivity.[16–19] For example, Pt-functionalized MoS_2 sensors have achieved sub-ppm detection limits for ammonia (NH_3) with rapid response and recovery, illustrating the potential of surface functionalization strategies.[16]

Similarly, MXenes—2D transition metal carbides and nitrides—have emerged as promising candidates for gas sensors due to their metallic conductivity, hydrophilic surfaces, and rich surface chemistry. $Ti_3C_2T_x$ MXene composites with conductive polymers such as polyaniline have demonstrated ultra-low detection limits and excellent cycling stability for toxic gases like NO_2, highlighting their potential for practical applications.[19] The ability to tune surface terminations in MXenes further enhances their selectivity and sensitivity.

Despite these advances, challenges remain in balancing sensitivity, selectivity, and long-term stability, particularly as many 2D sensors rely on chemical functionalization that may degrade over time.[17] In contrast, GNRFETs offer intrinsic advantages by leveraging electrostatic gating and quantum confinement effects, enabling highly tunable and reproducible sensing responses without extensive surface modification.[16,17] The gate-controlled modulation of carrier density in GNR channels allows dynamic adjustment of electronic properties in response to gas adsorption, providing an alternative pathway to enhance selectivity and sensitivity.

Graphene as a 2D material has emerged as a promising class of gas-sensing material. Its distinctive properties, including a large surface-to-volume ratio, high surface reaction activity, and excellent gas adsorption performance, have made it an attractive option for various sensing applications. The atomically thin and flat surface of 2D materials provides a large surface area for gas interaction, enhancing the sensitivity and selectivity of the sensing process.[20] Graphene can detect even a single gas molecule nearby because of its extremely low intrinsic electrical noise.[21]

Graphene transistors typically have sensitivity ranges between parts per billion (ppb) and parts per million (ppm),[22–24] and, with this sensitivity compared to solid-state sensors, graphene transistors have the potential to be a contender for the detection of a variety of chemicals, hazardous substances, biomolecules, and gases. Using sensitive devices is essential for detecting and monitoring gaseous threats that are difficult to perceive through our own senses or the naked eye. Among these various types of gases, ammonia (NH_3) is a toxic and hazardous gas that requires close monitoring in industrial, medical, and residential settings. Due to its harmful nature, the presence of ammonia must be closely tracked and managed across a variety of environments where human health and safety could be impacted.[25] In order to develop highly effective ammonia (NH_3) sensors capable of operating at room temperature, scientific researchers have explored a diverse array of materials for NH_3 gas detection. These materials include conducting polymers, metal oxides, carbon nanotubes, graphene, transition metal sulfides, and others.[26,27]

In terms of chemical properties, graphene also shows very high chemical stability, low power consumption, high speed response time (sensor response in less than 10 s), and short recovery time.[28] In addition, experimental research has indicated that the graphene sensor detects various gas molecules, such as CO, NO_2, H_2O, and NH_3 at room temperature.[29–31]

Drawing on previously developed analytical models of GNRFET characteristics,[28,32] this work presents a novel application of lanthanum aluminate ($LaAlO_3$) as a high-κ dielectric in GNRFETs, focusing on ammonia (NH_3) gas sensing. Although high-κ dielectrics such as HfO_2 are widely used in FETs, the integration of $LaAlO_3$ in GNRFET-based sensors remains underexplored. $LaAlO_3$ offers superior electrostatic control and enhanced device performance. The study further distinguishes itself by employing a double-gate

architecture, which, combined with $LaAlO_3$, significantly improves NH_3 sensitivity. This integrated approach systematically correlates device geometry and dielectric selection with gas-sensing performance, addressing limitations in prior studies that often considered these factors separately or targeted digital logic applications. By integrating double-gate engineering, high-κ dielectric materials, and sensing functionality within a unified platform, this work proposes a comprehensive design strategy to optimize sensor performance. Furthermore, the focused investigation of NH_3 detection fills a notable gap in GNRFET applications, extending their utility beyond conventional electronic devices. Collectively, these contributions represent a significant advancement in graphene-based sensor technology.

A rigorous numerical analysis of a double-gate GNRFET architecture, incorporating both top and back gates, has been conducted to achieve enhanced electrostatic channel control, thereby optimizing sensitivity and dynamic response. A comprehensive analytical model for the drain-source current has been developed, capturing intrinsic device behavior and perturbations induced by NH_3 exposure.

The electrostatic potential profile along the channel is obtained via a self-consistent solution of the 2D Poisson equation, explicitly accounting for short-channel effects and carrier distributions at the source and drain contacts. Current–voltage (*I*–*V*) characteristics have been derived over multiple operational regimes, initially excluding and subsequently incorporating the effects of gas adsorption and temperature variations to accurately reflect their impact on device performance.

The results systematically explore the modulation of drain current by gate and drain biases under both baseline and NH_3-exposed conditions. The influence of back-gate voltage, gate dielectric thickness, and gas concentration on the device's *I*–*V* response has been elucidated. Additionally, the effects of gate voltage, gate length, and dielectric permittivity on the I_{on}/I_{off} ratio were thoroughly examined, providing critical insights into the design and optimization of high-performance GNRFET-based gas sensors.

FET-Based Structure

As shown in Fig. 1, the suggested GNRFET's structure is relatively similar to that of a typical metal–oxide–semiconductor field–effect transistor (MOSFET) with double gates. It consists of source and drain electrodes connected by a graphene channel and a top-gate electrode that controls the carrier flow within the channel. A dielectric layer separates the top gate from the channel; in order to optimize electrostatic control and reduce short-channel effects, the gate partially covers the channel. The gate's primary function in a gas sensor is modulating channel conductivity, not an absorbing gas.[33] Materials like $LaAlO_3$ are used for the gate to enhance gas attraction to the channel, even though the gate partially covers it.

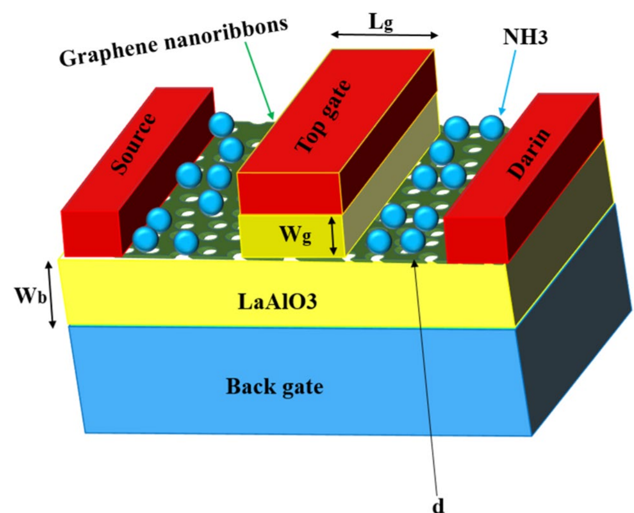

Fig. 1 Schematic of GNRFET structure.

In the presented structure, a dielectric layer separates the gate and the channel and a silicon back gate to increase carrier density or adapt the threshold voltage.[1–3] For low-power and high-transconductance applications, a high-*k* dielectric material, lanthanum aluminate, $LaAlO_3$, with a dielectric constant (*k*) of 30, is employed, due to its unique advantages, and, compared to HfO_2 and Al_2O_3 , it offers excellent interface quality with graphene, reducing charge traps that can degrade sensor performance. Furthermore, $LaAlO_3$ can potentially reduce leakage currents better than other materials and improve the overall performance of the GNRFET gas sensor.[34]

The asymmetric double-gate structures in GNRFET gas sensors offer several advantages. Varying the gate insulator thicknesses provides enhanced electrostatic control over the channel, improving performance, particularly in the sensitive subthreshold regime. Also, the thicker insulator helps to reduce the short-channel effects, minimizing leakage and improving stability. Thus, this design allows for optimized sensitivity and faster response times by fine-tuning the electric field distribution for different target gases.[35]

To detect ammonia gas, the device operates by exposing the regions between the source and gate, as well as the drain and gate, to the ambient air. This exposure allows the gas molecules to adsorb onto the graphene surface, which alters the concentration of charge carriers within the graphene. This alteration in charge carrier concentration translates directly into a measurable change in the drain–source current. The change in electrical current empowers the GNRFET device to function as a sensitive gas sensor.

Current Model

In this study, the electron gas within the channel is assumed to be non-degenerate, a simplification that is well founded under room temperature operation and moderate doping concentrations characteristic of the GNRFET device. However, under conditions of elevated doping or reduced temperature, the electron gas may transition into a degenerate regime. Accurately modeling this degenerate behavior is imperative to improve the fidelity of performance predictions and to extend the applicability of the model across a broader range of operating conditions.

Accordingly, the electron and hole distribution functions within the sub-bands near the source and drain electrodes are expressed as[36]:

$$\varepsilon_{p,n}^{-1} = \pm v\sqrt{P^2 + (\pi\hbar/d)^2} \tag{1}$$

Our device architecture utilizes a double-gate GNRFET with a 2.06-nm-wide nanoribbon channel (d = 2.06 nm), yielding a bandgap of 0.72 eV, as shown in Fig. 2. While this calculated bandgap corresponds to an ideal, defect-free GNR, it is important to acknowledge that practical fabrication processes introduce edge roughness, atomic-scale defects, and variability that can significantly influence the electronic properties of GNRs. Edge roughness and defects act as scattering centers and localized states, which may cause fluctuations in the bandgap, degrade carrier mobility, and lead to variability in device performance, including reduced ON/OFF current ratios and increased noise. Experimental investigations have reported these effects, highlighting the challenges in achieving uniform and reliable GNR devices. To mitigate these issues, advanced fabrication techniques such as bottom–up chemical synthesis and high-resolution lithographic patterning have been developed, enabling the production of GNRs with smoother edges and fewer defects. Incorporating these fabrication considerations provides a more comprehensive understanding of the practical limitations and guides future efforts toward realizing high-performance GNR-based devices.

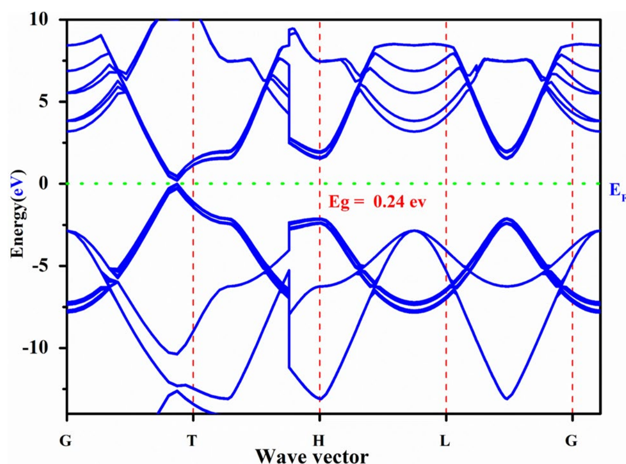

Fig. 2 Energy band structure of the GNR used in our structure.

The electronic transport is characterized by the parameters: charge carrier velocity, $v = 10^8$ cm/s, momentum along the nanoribbon (P), and the reduced Planck constant ($\hbar$). This configuration enables precise modeling of NH_3 gas-sensing mechanisms through charge transfer interactions at the graphene surface.

The proposed model establishes a relationship between the current, gas concentration, and temperature, expressed as:

$$I_{\text{GAS - GNR}} = I_{wg} + I_{gT} + I_{gF} \tag{2}$$

where I_{wg} represents the device current in the absence of gas exposure, incorporating the influence of the device's geometric parameters, I_{gT} denotes the temperature-dependent variation in the current and I_{gF} represents the modulation of the device current as a function of varying gas concentration, evaluated under constant temperature conditions. This term captures the influence of gas adsorption on carrier density and transport properties, thereby affecting the overall conduction behavior of the device.

The conductivity of the gas sensor varies as a function of both ammonia (NH_3) concentration and temperature, as reported in Refs. 37, 38.

The conventional top gate is substituted by the active region of the GNRFET, which is geometrically defined as

$$L_g/2 \le x \le L_g, \quad 0 \le z \le W_b,$$

where L_g denotes the length of the top gate along the nanoribbon axis (nm) (x-direction), which is an important parameter for short channel effect and carrier transport in GNRFETs, and W_b represents the thickness of the dielectric layer between the graphene channel and the back gate (nm) (z-direction) which is responsible for modulating the channel potential from below the substrate. Here, the x-axis is directed along the nanoribbons, whereas the z-axis is directed perpendicular to the nanoribbons and gate planes. This spatial domain corresponds to the portion of the device channel directly modulated by the gate potential, governing the carrier transport characteristics within the GNRFET.

To determine the potential distribution along the channel, the 2D Poisson equation is employed, expressed as[36]:

$$\frac{W_b + W_g}{3}\frac{\partial^2\varphi}{\partial x^2} - \frac{\varphi - V_b}{W_b} - \frac{\varphi - V_g}{W_g} = \frac{4\pi e}{\partial e}\left(\Sigma_- - \Sigma_+\right) \tag{3}$$

where φ denotes the electrostatic potential distributed along the channel, Σ_- and Σ_+ denote the electron and hole densities within the graphene channel, respectively, representing the concentration of negative and positive charge carriers contributing to conduction, e refers to a single electron carrying the elementary charge of an electron (Coulombs), a fundamental constant representing the magnitude of electric charge, æ refers to the dielectric constant of the material separating the graphene channel from the back gate (F/m), characterizing the material's ability to store electrical energy in an electric field, and $_{\mathrm{g}}$ represents the thickness of the insulating layer between the graphene channel and the top gate (nm), which influences the capacitive coupling and electrostatic control of the channel.

Electrostatic Modeling and Boundary Conditions in GNRFET

In our GNRFET simulations, the electrostatic potential distribution within the GNR channel is obtained by solving the two-dimensional (2D) Poisson equation

$$\nabla \cdot (\varepsilon \nabla \varphi) = -\rho,$$

where φ is the electrostatic potential, ε is the dielectric permittivity, and ρ is the net charge density in channel.[39]

Boundary Conditions

Source and Drain Contacts (Dirichlet Conditions):

The nanoribbon segments adjacent to the source and drain contacts are highly conductive and effectively act as ideal electron reservoirs. Therefore, the electrostatic potential at the source and drain edges of the channel (boundary conditions) is fixed as

$$\varphi|_{x=-L_{\mathrm{g}}/2} = 0 \text{ (Source)}, \varphi|_{x=L_{\mathrm{g}}/2} = V_{\mathrm{d}} \text{ (Drain)},$$

where L_{g} is the gate length and V_{D} is the applied drain voltage. This boundary condition ensures consistent alignment of the potential with the applied bias and sets the Fermi levels at the contacts.[40]

The nanoribbon segments adjacent to the source and drain contacts exhibit high conductivity and function effectively as conducting pads. Consequently, the electrostatic potential in these regions is fixed at $\varphi = 0$ near the source and $\varphi = V_{\mathrm{d}}$ near the drain terminal.

Lateral Edges of the Nanoribbon (Neumann Conditions)

Along the width of the graphene nanoribbon, Neumann boundary conditions are applied assuming a zero normal electric field

$$\left.\frac{\partial \phi}{\partial y}\right|_{\mathrm{edges}} = 0,$$

reflecting the physical confinement and absence of charge flow perpendicular to the channel edges.[39]

Gate Interfaces (Dirichlet or Mixed Conditions)

The top- and back-gate dielectrics impose fixed potentials corresponding to the applied gate voltages. These are incorporated as boundary conditions at the dielectric interfaces, enabling electrostatic control of the channel potential.[41]

Self-Consistent Calculation of Charge Densities Σ^+ and Σ^-

The electron (Σ^+) and hole (Σ^-) sheet charge densities in the GNR channel are computed self-consistently with the electrostatic potential. They depend on the local potential $\varphi(x, y)$ and the Fermi energies at the contacts $E_{\mathrm{F,S}}$ and $E_{\mathrm{F,D}}$, which are set by the source and drain voltages.

Specifically, Σ^+ and Σ^- are calculated by integrating the graphene nanoribbon density of states weighted by the Fermi–Dirac distribution

$$\Sigma^{\pm}(x, y) = \int D(E) f\left(E - E_{\mathrm{F}}(x, y)\right) \mathrm{d}E,$$

where $D(E)$ is the energy-dependent density of states of the GNR, and

$$E_F(x, y) = E_{\mathrm{F,contact}} - q\varphi(x, y)$$

accounts for local band bending due to the electrostatic potential.[40,42]

Electrostatics Near the Contacts

At the source and drain contacts, the Fermi levels are pinned by the metal–GNR interface, and the potential is fixed by applied bias. The carrier injection and extraction are modeled by setting the boundary potentials as described above. The charge densities $\Sigma^{\pm}$ transition sharply near the contacts, consistent with quantum transport simulations, ensuring accurate representation of contact electrostatics.[40]

Equation 3 governs the electric potential distribution within the device. This formulation facilitates analytical examination of non-uniform potential profiles across the GNRFET channel and enables rigorous assessment of short-channel effects. The electron densities at the source and drain regions are explicitly related to Fermi energies, local electrostatic potential, and fundamental physical parameters through:

$$\Sigma_{\pm}^{S} = \frac{2\sqrt{2\Delta K_{\mathrm{B}}T}}{\sqrt{\pi}\hbar d v}\exp\left(\pm\frac{\varepsilon_f^S + e\varphi}{K_{\mathrm{B}}T} - \frac{\Delta}{2}K_{\mathrm{B}}T\right)$$
$$\Sigma_{\pm}^{D} = \frac{2\sqrt{2\Delta K_{\mathrm{B}}T}}{\sqrt{\pi}\hbar d v}\exp\left(\pm\frac{\varepsilon_f^D + e(\varphi - V_d)}{K_{\mathrm{B}}T} - \frac{\Delta}{2}K_{\mathrm{B}}T\right) \tag{4}$$

where the corresponding value of the energy bandgap is defined as $\Delta = 4\pi\hbar/d$.

Assuming that the potential barrier formed at the interface between the electrodes and the GNR predominantly governs charge transport, the current per unit channel length can be expressed by[36]:

$$I_{wg} = \frac{2e}{\pi\hbar d}\left(\int v_p f_p^S \mathrm{d}p - \int v_p f_p^D \mathrm{d}p\right) \tag{5}$$

where

$$v_p = \frac{\mathrm{d}\varepsilon_{p,0}^{+}}{\mathrm{d}P} = v^2\frac{P}{\sqrt{v^2P^2 + \Delta^2/4}} \tag{6}$$

where v_p denotes the electron velocity corresponding to momentum p within the conduction band of the graphene nanoribbon, and the distribution functions f_p^d and f_p^s a represent the Fermi–Dirac occupation probabilities at the drain and source contacts, respectively, with their Fermi energies referenced relative to the mid-gap energy level.

Integration of Eq. 5 leads directly to the result presented in[36]:

$$I_{wg} \propto \begin{cases} \frac{Vgs + \frac{V_b \cdot W_g}{W_b}}{W_b + W_g} \cdot \left(1 - \frac{1}{\cosh\cosh\left(\frac{L_g}{2\Lambda}\right)}\right) + \frac{V_d}{2\cosh\cosh\left(\frac{L_g}{2N}\right)}; & \text{at } \left|V_g\right| > V_b W_g / W_b \\ \frac{Vgs \cdot W_b}{W_b + W_g} \cdot \left(1 - \frac{1}{\cosh\left(\frac{L_g}{2\Lambda}\right)}\right) \cdot \left(1 + \frac{W_b}{W_b + W_g} \cdot \frac{1}{e \cdot \frac{V_b}{K_b . T}}\right); & \text{at } \left|V_g\right| \le V_b W_g / W_b \end{cases} \tag{7}$$

where $\Lambda = \sqrt{(W_b/3)}$ denotes the effective screening length.

The Current with Gas Exposure

The parameters IgT and IgF can be correlated and expressed as a single interdependent parameter, as described in[30]:

$$I_{\mathrm{Gas}} = I_{gT} + I_{gF} = \frac{2e}{\pi\hbar d}\left(\int\left(\frac{x^{-2}}{1 + e^{x-\eta}}\mathrm{d}x + \frac{x^{-2}}{1 + e^{x+\eta}}\mathrm{d}x\right)\right) \tag{8}$$

where $\eta = (E_F - E_{\mathrm{G}})/k_{\mathrm{B}}T$ and $x = (E - E_{\mathrm{G}})/k_{\mathrm{B}}T$ are the normalized Fermi energy. Numerical resolution of this equation is performed using the partial integration method.[38,43]

Accordingly, the general current model for this component of the graphene-based gas sensor can be derived analogously to the silicon-based model introduced by Gunlycke et al.[44]:

$$I_{\mathrm{Gas}} = \frac{2e}{\pi\hbar d}\left(\xi_{-1/2}\frac{E_{\mathrm{F}} - E_{\mathrm{G}}}{K_{\mathrm{B}}T} + \xi_{-1/2}\frac{E_{\mathrm{G}} - E_{\mathrm{F}}}{K_{\mathrm{B}}T}\right)V_{gs} \tag{9}$$

where $\xi - 1/2$ is the Fermi–Dirac integral of order (− ½) which plays a significant role in the modeling of a semiconductor's behavior, and E_{G} strongly influences the gas sensor conductance because it depends on gas concentration and its temperature, [37] which can be expressed as[45]:

$$E_{\mathrm{G}} = \delta T + \lambda F,$$

where the temperature-controlling parameter is denoted by δ, representing the sensitivity of the energy bandgap to temperature changes, λ is the gas concentration-monitoring parameter, representing the modulation of the energy bandgap due to gas adsorption, while F denotes the gas concentration, quantifying the amount of gas interacting with the graphene nanoribbon. These parameters describe the dependence of the energy bandgap on temperature and gas concentration, respectively. They were originally introduced and derived in earlier studies on carbon nanotube field-effect transistors (CNTFETs), which share similar physical principles with GNRFETs. A notable example is the semi-empirical modeling approach presented by Marani and Perri,[46] where the temperature dependence of the energy bandgap

is incorporated into the I–V characteristics of CNTFETs. The iteration method is used to acquire these parameters.[47]

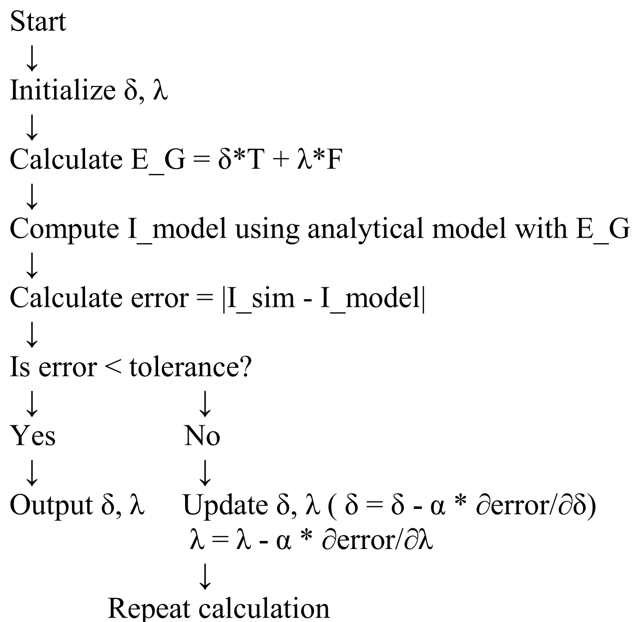

Flowchart of the Iterative Extraction Process

The gas sensor current model has been derived from Eqs 9 and 10 and is expressed as:

$$I_{Gas} = \frac{2e}{\pi\hbar d}\left(\xi_{-1/2}\frac{E_F - (\delta T + \lambda F)}{K_B T} + \xi_{-1/2}\frac{(\delta T + \lambda F) - E_F}{K_B T}\right)V_{gs} \tag{10}$$

By combining Eqs. 7 and 10 and applying the relevant equations, a general expression for the source-drain current is derived based on the top-gate voltage, channel length, gas concentration, and temperature.

This comprehensive formulation enables a detailed analysis of the performance of the graphene-based gas sensor FET across diverse operational conditions, offering valuable insights into the influence of key parameters on sensor efficiency and responsiveness:

$$I_{\text{Gas-GNR}} = v\left(\frac{æ}{2\pi^{3/2}\cdot Wb}\right)\left(\sqrt{\frac{K_B\cdot T}{\delta}}\exp\left(\frac{e\cdot\varphi_m}{K_B\cdot T}\right)V_b - (V_b - V_{ds})\exp\left(-\frac{e\cdot Vds}{K_B\cdot T}\right) - \left(\frac{6q^2}{\hbar L_g}\right)(3a_{cc}tK_BT)^{1/2}\left(\frac{2}{\sqrt{\pi}}\sqrt{\frac{E_F - E_G}{K_BT}}\left(\frac{E_F - E_G}{K_B\cdot T}\right) + \frac{2}{\sqrt{\pi}}\sqrt{\frac{-E_F + E_{GG}}{K_BT}}\left(\frac{E_F - E_G}{K_B\cdot T}\right)\right)(V_{gs} - V_{th})\right) \tag{11}$$

To assess the performance of graphene-based gas sensor FET devices, a specific equation derived from the I–V characteristics has been employed. By monitoring the top-gate voltage, which varies in response to gas exposure, the drain–source current can be effectively controlled.

Our model functions analogously to conventional MOSFET devices, operating within both the ohmic and saturation regimes. This framework highlights the versatility of graphene as a material for improving gas sensor performance. However, while the assumption of a non-degenerate electron gas simplifies the analysis of GNRFET-based gas sensors, it may not fully capture the complex electronic behavior inherent to graphene under all conditions.

This model exhibits limitations under conditions of high doping concentrations and low temperatures. Nevertheless, it remains valid and provides accurate predictions when the GNRFET operates at room temperature with moderate doping levels, where the electron gas can be reasonably approximated as non-degenerate. This assumption enables more straightforward analytical and numerical modeling, providing valuable insights into general trends without excessive computational complexity. Therefore, while simplifying analysis, the non-degenerate electron gas assumption's limitations at high doping levels or low temperatures must be considered for accurate performance predictions.[43,48,49]

Simulation Framework and Numerical Implementation:

The electrostatic potential distribution was obtained by solving the 2D Poisson equation using the finite difference method on a uniform spatial grid. An iterative successive over-relaxation technique was employed to accelerate convergence, with the relaxation factor optimized around 1.8. The convergence criterion was set to a relative residual below 10^{-6}, ensuring numerical accuracy. As the simulations consider steady-state conditions, time-dependent integration was not involved.

All the simulations were performed using MATLAB R2023a. The computational framework relies primarily on built-in MATLAB functions, without the need for specialized toolboxes, while custom-developed scripts were implemented for discretization, matrix assembly, and iterative solution of the governing equations.

Boundary conditions were carefully imposed as follows. Dirichlet boundary conditions fixed the electrostatic potential at the source and drain contacts to the applied bias voltages. The gate voltage was incorporated via a fixed potential boundary at the gate dielectric interface. Neumann boundary conditions (zero normal derivative) were applied at the lateral edges of the simulation domain, representing insulating boundaries and preserving charge neutrality. These

boundary conditions are consistent with established quantum transport modeling approaches for GNRFETs.

A uniform mesh grid with a spatial discretization of 0.1 nm along both the channel length and width directions was employed. This fine mesh resolution was selected to accurately capture quantum confinement effects and potential variations within the GNR channel.

Results and Discussion

This section presents the simulation results for the GNRFET. The *I–V* characteristics are systematically analyzed to elucidate the impact of key parameters on device performance.

These findings offer critical insights into the operational behavior of the GNRFET under varying conditions, underscoring its promising potential for applications in gas sensing and related technological domains.

Figure 3 presents the *I–V* characteristics of the simulated GNRFET device, with specified dimensions of $L_g = 100$ nm, $W_g = 30$ nm, and $W_b = 70$ nm, both in the presence and absence of NH_3 gas exposure. The curves were measured for several gate voltages ($V_{gs} = 0.72$ V, 0.74 V, 0.76 V, 0.74 V, and 0.80 V). The observed behavior is characteristic of conventional FET transistors, wherein the drain current (I_{ds}) increases with the drain voltage (V_{ds}), eventually stabilizing at higher voltages. Notably, as the gate voltage increases, there is a corresponding enhancement in the drain current, indicating improved channel conductivity. Upon exposure to NH_3 gas at a concentration of 300 ppm, a significant increase in the drain current was observed across the various gate voltages tested. This increase can be attributed to the interactions between the NH_3 molecules and the graphene channel. Specifically, NH_3 acts as an electron donor, resulting in an elevated electron concentration within the device's active region. This enhancement in electron density leads to a marked increase in conductivity, facilitating a rise in the drain current from 10^{-7} A to 10^{-5} A. These findings highlight the efficacy of GNRFET transistors as high-quality NH_3 detectors. The observed substantial increase in drain current upon exposure to NH_3 gas quantitatively underscores the high sensitivity of the GNRFET, demonstrating its capacity to reliably transduce even minute variations in ambient NH_3 concentration. This robust response positions the GNRFET as a compelling candidate for high-performance gas sensing applications, notably in critical domains such as environmental surveillance, industrial process control, and advanced safety systems. Consistent results have been reported in prior studies.[50,51]

The sensitivity of the GNRFET is quantified by the percentage change in current upon exposure to the target gas, which can be calculated through:

$$S = \frac{(I_g - I_{wg}) \times 100}{I_{wg}} \tag{12}$$

where I_g is the drain current measured with gas exposure, and I_{wg} is the baseline drain current without gas exposure. This formulation provides a normalized and intuitive measure of sensor response, a definition that is consistent with approaches commonly used in graphene- and carbon nanotube-based sensor literature, [52–54] where sensitivity is expressed as a normalized change in an electrical parameter to facilitate comparison across different sensor platforms.

As shown in Fig. 4, the results indicate that, upon exposure to 450 ppm NH_3, the sensitivity increased by 120% at $V_g = 0.8$ and $T = 300$ K.

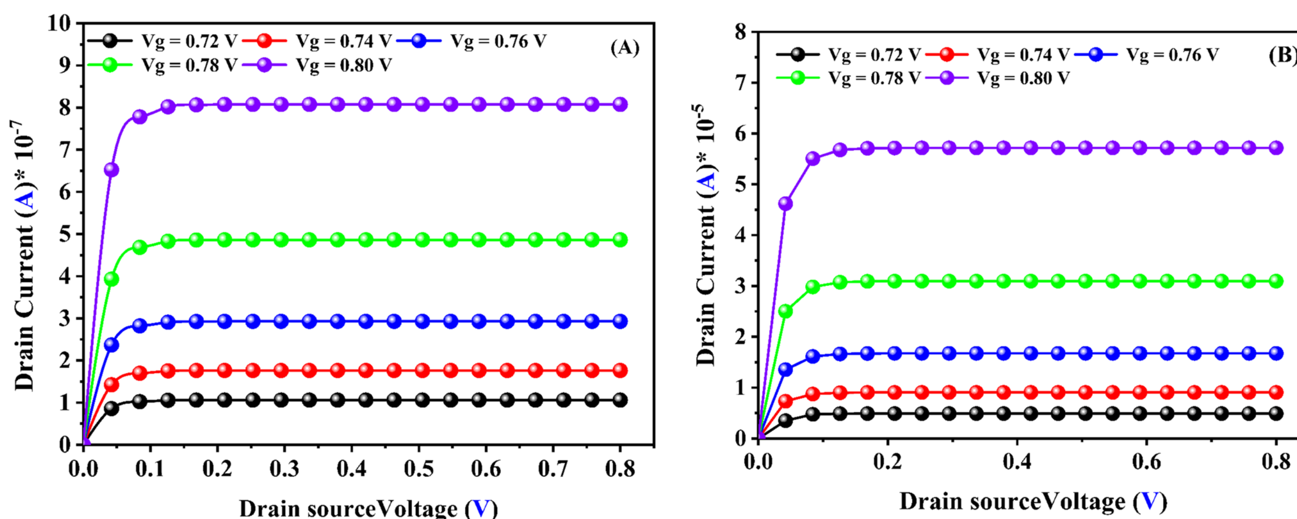

Fig. 3 *I–V* characteristics: (a) without NH_3 exposure, and (b) with NH_3 exposure where NH_3 concentration $F = 300$ ppm.

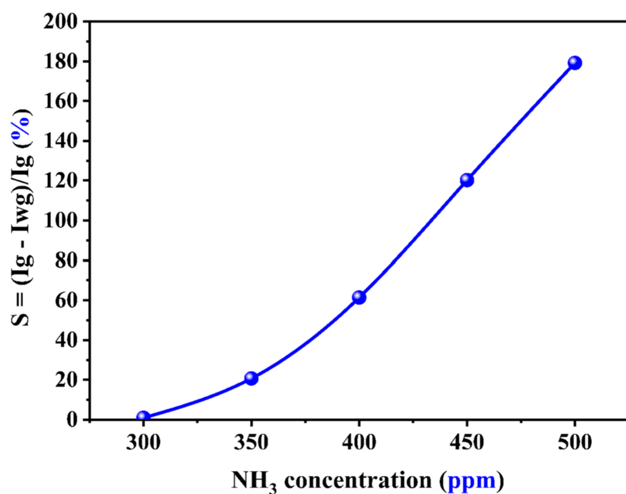

Fig. 4 Effect of NH_3 concentration on sensitivity.

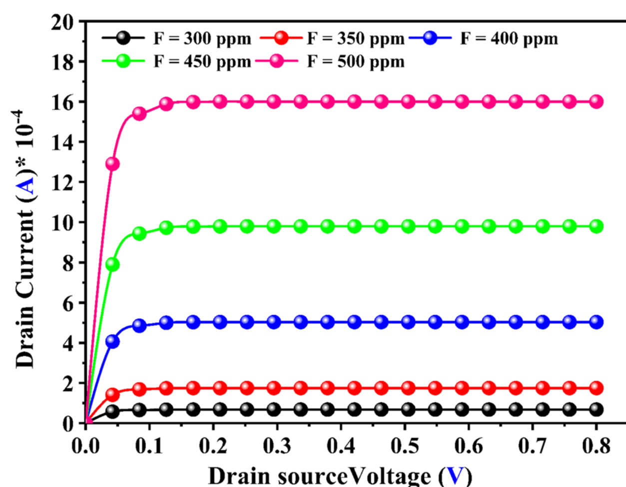

Fig. 5 I_{ds} vs. V_{ds} characteristics of GNRFET transistor for different NH_3 gas concentrations at room temperature $T = 300$ K.

The sensor's sensitivity demonstrates almost linear behavior, which may be attributed to the significant transformation of the Schottky junctions formed between the GNR and the electrodes.

Notably, our structure achieves a sensitivity of approximately 120% at 450 ppm, exhibiting enhanced sensitivity relative to basic GNRFET gas sensor designs that achieves only 55% at 450 ppm, thus demonstrating superior sensitivity to NH_3. The CNT/ rGO-Am sensor[50] also exhibits an excellent sensitivity to NH_3. This comparison underscores the superiority of nanomaterial-based sensors for high-sensitivity applications.

Figure 5 depicts the *I–V* characteristics of the GNRFET device measured at room temperature (300 K) with a fixed gate bias of 0.7 V, following exposure to varying concentrations of ammonia (NH_3) gas (300 ppm, 350 ppm, 400 ppm, 450 ppm, and 500 ppm). The data reveal a systematic and concentration-dependent increase in the drain current upon NH_3 exposure, indicative of enhanced charge carrier modulation within the GNR channel. This pronounced response underscores the device's high sensitivity and effective transduction mechanism for NH_3 detection, attributable to charge transfer interactions that alter the channel conductivity. The observed trends confirm the potential of the GNRFET as a robust platform for selective and sensitive gas-sensing applications. This enhancement in device performance can be attributed to charge transfer interactions between the adsorbed NH_3 molecules and the graphene channel. Specifically, NH_3 functions as an electron donor, leading to an increase in electron concentration within the *n*-type GNR. Consequently, as the NH_3 concentration increases, a greater number of electrons are transferred to the channel, thereby augmenting its conductivity and modulating the transistor's electrical response. Consequently, this increased charge carrier density leads to a marked increase in the drain current (I_{ds}), demonstrating the phenomenon of chemical doping facilitated by gas molecules.[55]

The results demonstrate that the GNRFET transistor exhibits a clear and consistent response to varying concentrations of NH_3 gas, as evidenced by the measurable changes in current. This pronounced sensitivity across the tested concentration range highlights the transistor's capability to effectively detect NH_3, indicating its strong potential for applications in environmental monitoring and gas-sensing technologies. The observed current modulation with increasing NH_3 levels confirms the device's suitability for reliable and sensitive gas detection. The present study focuses on NH_3 concentrations in the range of 300–500 ppm to effectively capture the fundamental charge transfer and transport mechanisms governing the device response. This concentration window aligns with prior theoretical and simulation investigations, such as those by Tamersit et al.[50]and Mahmoudi et al.[51] , enabling direct comparison and validation of our findings. While detection at lower concentrations, particularly in the ppb range, is essential for many practical applications, modeling sensor behavior at these levels involves additional complexities. These include weak physisorption interactions, stochastic adsorption–desorption kinetics, and intrinsic device noise, which require advanced multi-scale modeling beyond the scope of the current work. Future efforts will focus on extending the simulation framework to incorporate these effects, thereby enabling exploration of the sensor's detection limits and sensitivity at lower NH_3 concentrations. Such advancements will further enhance the practical applicability of GNRFET-based gas sensors in real-world scenarios (Tables I, II, and III).

This makes GNRFET an effective tool for real-time sensing of NH_3, which is crucial for applications in various

Table I Electrical parameters of our GNRFET structure

Parameter	Description
$\Sigma_{\pm}^{S/D}$	The electron densities (electron/hole flux) at source/drain contacts (cm^{-2})
$\varepsilon_{f}^{S/D}$	Fermi energy levels at source/drain contacts
φ	Electrostatic potential in the channel (V)
V_d	Drain voltage bias (V)
Δ	Energy bandgap of graphene nanoribbon (eV)
v	Carrier velocity or attempt frequency (cm/s)
K_b	Boltzmann constant (m^2 kg^{-2} K^{-1})
$\hbar$	The reduced Planck constant
e	Elementary charge (Coulombs)
T	Absolute temperature (Kelvin (K))

Table II Necessary parameters for the suggested structure's design

Device parameters	Value
GNR type	Armchair
GNR bandgap energy	0.72 eV
Graphene channel width	2.06 nm
Gate length (L_g)	100 nm
Thickness of the top-gate dielectric (W_g)	30 nm
Thickness of the back-gate dielectric (W_b)	70 nm
Dielectric constant (k)	30
Temperature (T)	300

industries, including agriculture and environmental science, [56] noting that the prolonged exposure to ammonia can adversely affect the long-term stability and structural integrity of GNRFET sensors through strong adsorption, slow recovery times, irreversible changes in electrical properties, and potential mechanical degradation. Ongoing research into passivation techniques and material modifications is essential for improving the resilience of these sensors in real-world applications.[57,58]

Figure 6 illustrates the *I–V* characteristics for various back-gate voltages (V_b = 1 V, 2 V, and 3 V) at room temperature, specifically under an ammonia (NH_3) concentration of F = 300 ppm. The data reveal a clear trend: as the drain voltage (V_{ds}) increases, the source–drain current (I_{ds}) also rises across all back-gate voltage settings, which can be attributed to the enhanced electron density within the graphene channel, induced by the application of the back-gate voltage. As the back gate voltage increases, it effectively modulates the electrostatic potential, increasing the charge carrier concentration in the channel. This enhanced electron density allows for a more substantial flow of electrical current when a drain voltage is applied, illustrating a direct positive correlation between the drain current and the back-gate voltage.

The gate-dependent response profiles reveal a critical decoupling of electrostatic control from adsorption sensitivity. Figure 6 demonstrates that, while the back-gate voltage (V_b) enhances baseline conductivity through global carrier density modulation, its negligible impact on sensitivity arises from the fundamentally different mechanisms governing gate electrostatics, and gas adsorption. Specifically, the back gate serves primarily for baseline electrostatic tuning across the channel, whereas NH_3 sensitivity is dictated by localized surface interactions on the exposed graphene region. As a result, the uniform electrostatic influence of V_b does not alter the charge transfer efficiency per adsorbed molecule, leading to a consistent relative current response across different gate voltages. In contrast, the top gate, although capable of strong electrostatic control, is fully encapsulated and thus remains decoupled from gas adsorption processes. This mechanistic separation informs the sensor design paradigm where surface engineering, not gate biasing, governs sensitivity optimization.

These results corroborate prior studies demonstrating the efficacy of GNRFETs as sensitive detectors for gases such as ammonia (NH_3). Notably, a sensitivity of approximately 2.7% has been reported following exposure to 1 ppm NH_3,[51] underscoring the capability of GNRFETs to transduce gas adsorption events into measurable electrical signals. This sensitivity is attributed to charge transfer interactions between NH_3 molecules and the GNR channel, modulating the device conductance. Although the influence of the back gate on sensor sensitivity is minimal, operating the GNRFET in the subthreshold regime can further enhance detection performance. Collectively, these findings highlight the promising potential of GNRFET-based architecture for low-power, high-sensitivity, gas-sensing applications.

Previous investigations have substantially deepened our understanding of the correlation between gate voltage and current in FETs. However, a critical factor has often been

Table III Comparing the sensitivity of our GNRFET gas sensors with other similar structures

Sensor type	Gas type	Concentration (ppm)	Sensitivity (%)	References
Our GNRFET gas sensor	NH_3	450	120	This study
GNRFET	NH_3	1	2.7	[51]
GNRFET	NH_3	450	55	[51]
CNT/rGO-Am sensor	NH_3	400	115	[85]

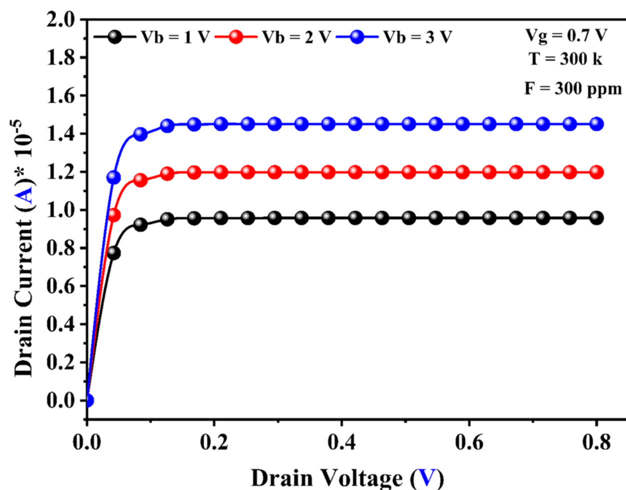

Fig. 6 *I–V* characteristics for different values of back-gate voltage.

neglected: the influence of the insulating layer thickness separating graphene from the gate electrodes specifically, the top gate (W_g) and back gate (W_b). This oversight is significant, as the dielectric layer's characteristics critically affect the electrostatic modulation of the channel, thereby directly impacting the drain current (I_{ds}). Figure 7 addresses this gap by depicting the variation of the drain current (I_{ds}) as a function of the drain voltage (V_{ds}). Specifically, Fig. a examines the influence of the insulating layer thickness between graphene and the top gate, while Fig. 7b focuses on the corresponding effect of the layer thickness between graphene and the back gate. The device was subjected to continuous exposure of NH_3 gas at a concentration of 300 ppm under ambient temperature conditions ($T = 300$ K), thereby providing a practical framework for evaluating its gas-sensing capabilities in realistic operational environments.

As the thickness of the back-gate insulation increases, there is a corresponding increase in the drain–source current (I_{ds}). This behavior can be attributed to the greater capacitance provided by a thicker insulating layer, which improves the electrostatic coupling between the back gate and the graphene channel. This enhanced coupling allows for better modulation of the charge carrier density in the graphene, leading to an increase in current flow. Conversely, increasing the thickness of the top-gate insulation results in a decrease in I_{ds}. This trend suggests that a thicker insulating layer weakens the electrostatic influence of the top gate on the graphene channel. Consequently, as the gate thickness increases, the ability of the gate voltage to effectively control the channel's carrier concentration diminishes, leading to reduced current conduction. This inverse relationship emphasizes the importance of gate design and material choice in optimizing device performance. Furthermore, the study also examined the effect of some parameters on the I_{on}/I_{off} ratio.

The effect of gate length on the I_{on}/I_{off} ratio was investigated, as shown in Fig. 8. This analysis was conducted on a GNRFET characterized by a permittivity of $k = 30$, a body width of $W_b = 70$ nm, and a gate width of $W_g = 20$ nm at a temperature of 300 K. The back-gate voltage (V_b) has been evaluated at two levels: 0.3 V and 0.7 V, while the drain voltage (V_{ds}) was maintained at a constant 0.4 V. The top-gate voltage varied between 0.72 V and 1.0 V. From Fig. 8, it can be observed that the current density exhibits an inverse relationship with respect to the back-gate voltage for fixed channel lengths. Specifically, as the back-gate voltage increases, the current density decreases. This behavior may be attributed to enhanced electrostatic control of the channel by the gate, which modulates carrier density and mobility. Moreover, with a specific back-gate voltage, there is a clear trend in which the current density

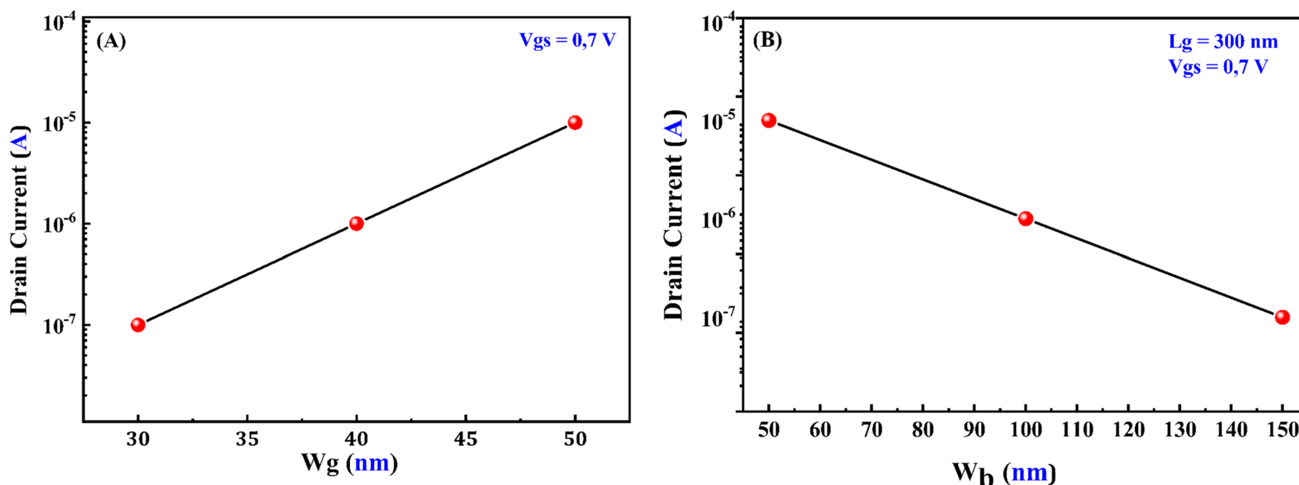

Fig. 7 Variation of I_{ds} versus V_{ds} for different thicknesses of the layer between graphene and (a) the top gate and (b) the back gate.

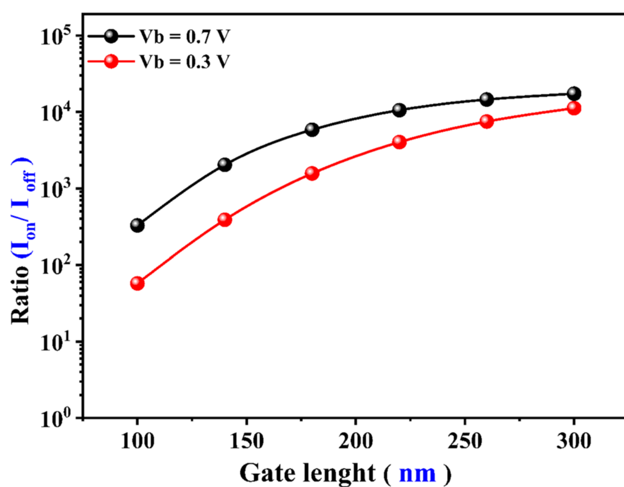

Fig. 8 Variation of I_{on}/I_{off} ratio as a function of gate length.

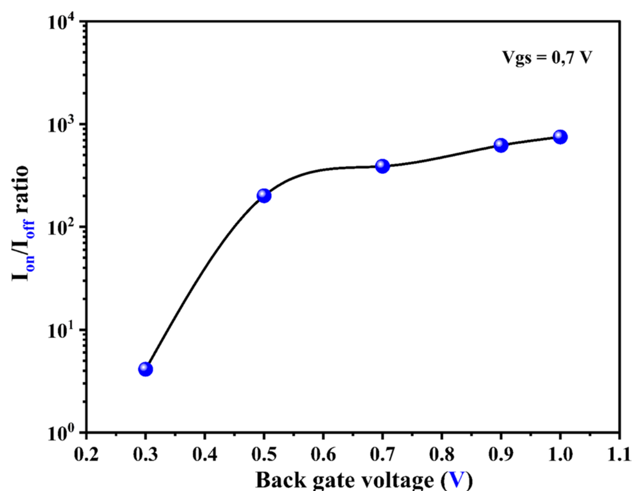

Fig. 9 Variation of the I_{on}/I_{off} ratio as a function of back-gate voltage (V_b).

decreases as the channel length increases. This inverse correlation highlights the importance of gate length in determining device performance; longer channel lengths lead to increased channel resistance, which results in reduced current flow.

Figure 9 shows the variation of the I_{on}/I_{off} ratio as a function of the back-gate voltage (V_b) in the GNRFET gas sensor. In our analysis, the back-gate voltage (V_b) was varied systematically over the range of values of 0.3 V, 0.5 V, 0.7 V, 0.9 V, and 1.0 V, while maintaining a fixed drain–source voltage, V_{ds} = 0.4 V This range of V_b values was chosen to comprehensively investigate the influence of the back-gate bias on the device characteristics, including the modulation of channel conductivity and the resulting I_{on}/I_{off} ratio. By exploring multiple back-gate voltages at a constant V_{ds}, we ensured a detailed understanding of the electrostatic control exerted by the back gate under typical operating conditions. Also, it was observed that the I_{on}/I_{off} ratio increased significantly with rising V_b. This enhancement can be attributed to the improved electrostatic control exerted by the back gate over the channel potential. As V_b increases, the gate-induced electric field more effectively modulates the carrier concentration in the GNR, shifting the Fermi level and altering the channel conductivity.

In particular, the off-state current (I_{off}) decreases due to a stronger depletion of carriers, which raises the potential barrier and suppresses leakage currents. Concurrently, the on-state current (I_{on}) increases as the channel becomes more conductive under higher gate bias, facilitating enhanced carrier injection and transport. The combined effect of reduced I_{off} and increased I_{on} leads to a pronounced improvement in the I_{on}/I_{off} ratio, which is critical for achieving high sensor sensitivity and low power operation.

This behavior is consistent with theoretical and experimental studies on GNRFETs, where enhanced gate control via back-gate biasing improves switching characteristics and amplifies the sensor response to adsorbed gas molecules. The increased I_{on}/I_{off} ratio under higher V_b conditions thus not only reflects better device performance but also contributes to improved detection capabilities by increasing the signal-to-noise ratio in the presence of gas analytes.

Figure 10a and b demonstrates the relationship between the on-state current, I_{on} and the I_{on}/I_{off} ratio as functions of gate dielectric permittivity at three distinct temperatures (T = 200 K, 300 K, and 400 K). The I_{on} values were measured with a gate–source voltage (V_{gs}) of 0.7 V and a drain–source voltage (V_{ds}) of 0.4 V, while I_{off} was defined as the current measured at V_{gs} = 0 V and V_{ds} = 0.4 V. An increase in gate dielectric permittivity correlates with a rise in the I_{on}/I_{off} ratio. This trend can be attributed to improved gate control over the channel, which facilitates more effective current modulation which means the changes in the electrical current flowing through the device. Specifically, higher permittivity enhances the electrostatic coupling between the gate and the channel, leading to an increase in I_{on} relative to I_{off}. Furthermore, temperature significantly influences both gate dielectric permittivity and the I_{on}/I_{off} ratio. As the temperature increases, the dielectric properties of the material may change, resulting in a higher I_{on}/I_{off} ratio at elevated temperatures. This observation indicates that thermal effects are critical for enhancing transistor performance, emphasizing the necessity of optimizing device parameters for varying operational conditions. However, temperature affects the CNTFET transistor inversely in the absence of NH_3.[59] At elevated temperatures, thermal energy facilitates the transfer of charge carriers between gas molecules and the GNRFET. When gas molecules adsorb onto the graphene surface, they can donate electrons to the GNRFET, altering its conductivity and increasing the drain current, thereby enhancing the

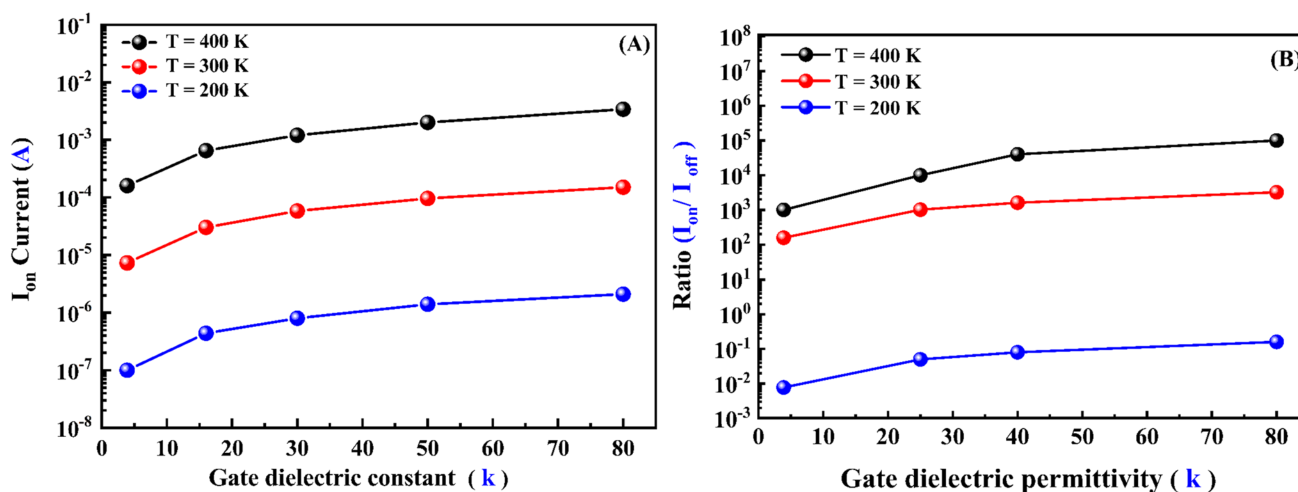

Fig. 10 (a) Variation of I_{on} as a function of gate dielectric permittivity, (b) variation of I_{on}/I_{off} ratio as a function of gate dielectric permittivity.

sensitivity of the device. The present simulations focus on intrinsic GNRs operating near room temperature. Accordingly, the non-degenerate electron gas approximation applied here is appropriate and consistent with the physical regime under study. Our model employs a self-consistent solution of the 2D Poisson equation coupled with carrier transport equations, accurately capturing the spatial distribution of electrostatic potential and charge density within the device channel. This framework inherently accounts for electrostatics without explicitly requiring treatment of electron degeneracy effects. While this approach is valid for the moderate doping and temperature conditions considered, extensions to regimes involving high doping concentrations or low temperatures would necessitate incorporation of Fermi–Dirac statistics to properly describe degenerate carrier populations. Future work will address these aspects to broaden the model's applicability. Clarifying these assumptions provides a clear understanding of the model's scope and limitations.

Figure 11 shows the drain current (I_{ds}) as a function of drain–source voltage (V_{ds}) for three temperatures: 300 K, 350 K, and 400 K, at a fixed gate voltage V_{gs} = 0.7 V and NH_3 gas concentration F = 300 ppm. As temperature increases, the drain current systematically rises for all values of V_{ds}. This increase in I_{ds} with temperature can be attributed primarily to enhanced carrier transport mechanisms in the GNR channel. Elevated temperature leads to increased thermal energy, which promotes carrier excitation and reduces the effective scattering from impurities and defects, thereby increasing carrier mobility in the channel.[60,61] Additionally, thermally activated processes can increase the intrinsic carrier concentration, contributing to a higher baseline conductivity.

The observed behavior aligns with prior studies on graphene FETs, where temperature elevation enhances the drain current due to increased carrier density and mobility before self-heating effects become dominant.[61] In our device, the temperature range up to 400 K remains below critical thresholds where significant self-heating or degradation occurs, ensuring that the current increase is dominated by intrinsic transport improvements rather than device damage.

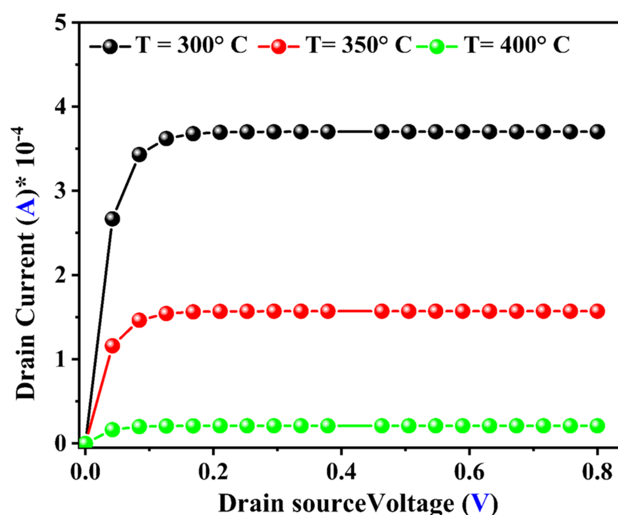

Fig. 11 Drain current I_{ds} variation with drain–source voltage (V_{ds}) at different temperatures (T).

Furthermore, the gas concentration of F = 300 ppm introduces NH_3 adsorption effects that modulate the local carrier density through charge transfer. While the adsorption-induced doping remains constant in this comparison, the temperature rise amplifies the overall conductivity, effectively increasing the measured I_{ds}, indicating that sensor operation at elevated temperatures could improve signal

levels, potentially enhancing detection sensitivity and the signal-to-noise ratio.

It is also notable that the slope of the I_{ds}–V_{ds} curves increases with temperature, indicating improved channel conductance and reduced resistance. This behavior suggests that, at higher temperatures, the channel approaches more linear transport characteristics over the measured voltage range, consistent with reduced carrier scattering and enhanced mobility.

In summary, the temperature-dependent increase of I_{ds} under fixed gate bias and gas concentration highlights the critical role of thermal effects on carrier transport in GNRFET sensors. These findings suggest that the operating temperature is an important parameter for optimizing sensor performance, balancing enhanced conductivity against potential thermal degradation at higher temperatures.

Figure 12 illustrates the variation of drain current density as a function of gate length, specifically examining two different top-gate thicknesses (W_g = 10 nm and 20 nm) for both ON and OFF states, labeled as (a) for I_{on} and (b) for I_{off}. It is evident that the drain's current density (J_d) decreases exponentially as the gate length increases. For instance, at gate lengths of 50 nm, 70 nm, and 100 nm, the observed current densities are 3×10^3 mA/cm^2, 4×10^{-1} mA/cm^2, and 3×10^{-3} mA/cm^2, respectively. This trend indicates a clear inverse correlation between current density (J_d) and gate length (L_g), underscoring that, as the gate length increases, the current density significantly diminishes.

Figure 12 demonstrates that the current density increases as the thickness of the insulating layer between graphene and the gate electrode is increased, indicating a direct correlation between layer thickness and device current performance, W_g = 20 nm, J_d gives higher values than W_g = 10 nm. The carrier density in a transistor is the number of charge carriers per unit area. When the gate width is increased, the number of charge carriers in the channel also increased. This is because the wider gate allows for more charge carriers to flow through the channel. This increased carrier density leads to a higher drain current and a higher current density. In contrast to the influence of gate length on current density, where an increase in gate length results in a decrease in current density, the relationship between gate length and the ON/OFF current ratio (I_{on}/I_{off}) exhibits a different trend. As illustrated in Fig. 10, increasing the gate length enhances the I_{on}/I_{off} ratio. Specifically, at a gate length (L_g) of 50 nm, the (I_{on}/I_{off}) ratio is observed to be 10^3 for a gate width (W_g) of 10 nm, while it increases significantly to 3×10^2 for a gate width of 20 nm. This demonstrates that optimizing the gate length can effectively improve the switching performance of the device by boosting the I_{on}/I_{off} ratio, which is crucial for achieving better device performance in applications.

In FETs such as MOSFETs, CNTFETs, and GNRFETs, transconductance (denoted as g_m) is a critical parameter that measures the device's ability to control the drain current through variations in the gate–source voltage. A higher g_m indicates improved current control, which is particularly important for amplifying changes in the drain current, especially when the device operates under the influence of external factors such as ammonia gas.

As illustrated in Fig. 13, increasing the dielectric constant leads to a substantial increase in the ON-state current, which consequently enhances the transconductance (g_m). $LaAlO_3$ was selected as the gate dielectric due to its superior interface quality with graphene, forming a clean and abrupt interface that minimizes charge traps and preserves graphene's high carrier mobility.[62] Compared to HfO_2 and Al_2O_3, $LaAlO_3$ offers enhanced dielectric reliability, attributed

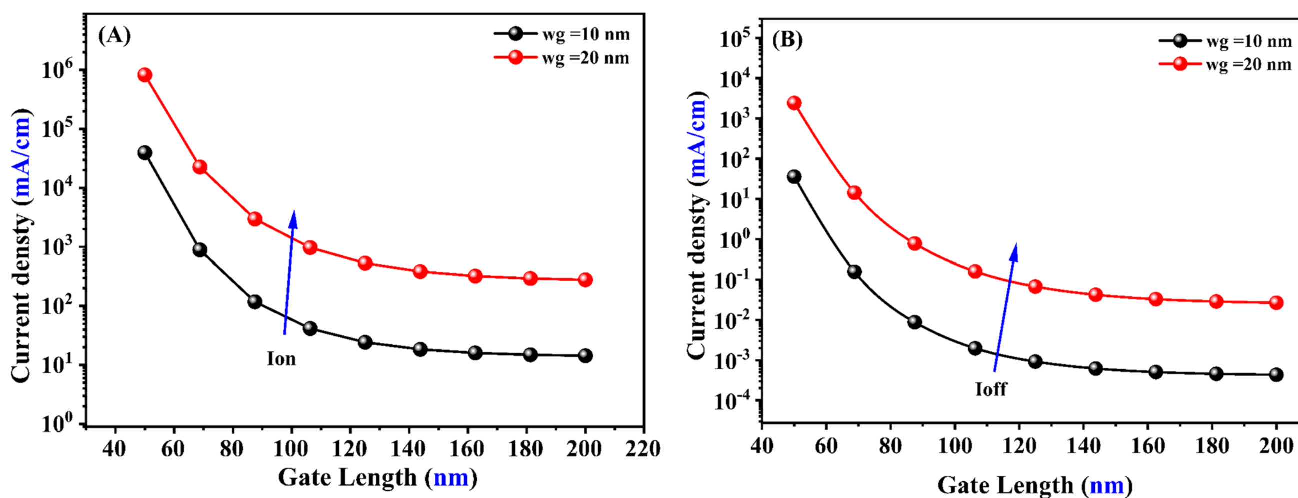

Fig. 12 Drain current density versus gate length for different thickness (W_g = 10 nm and 20 nm); (a) I_{on} and (b) I_{off}.

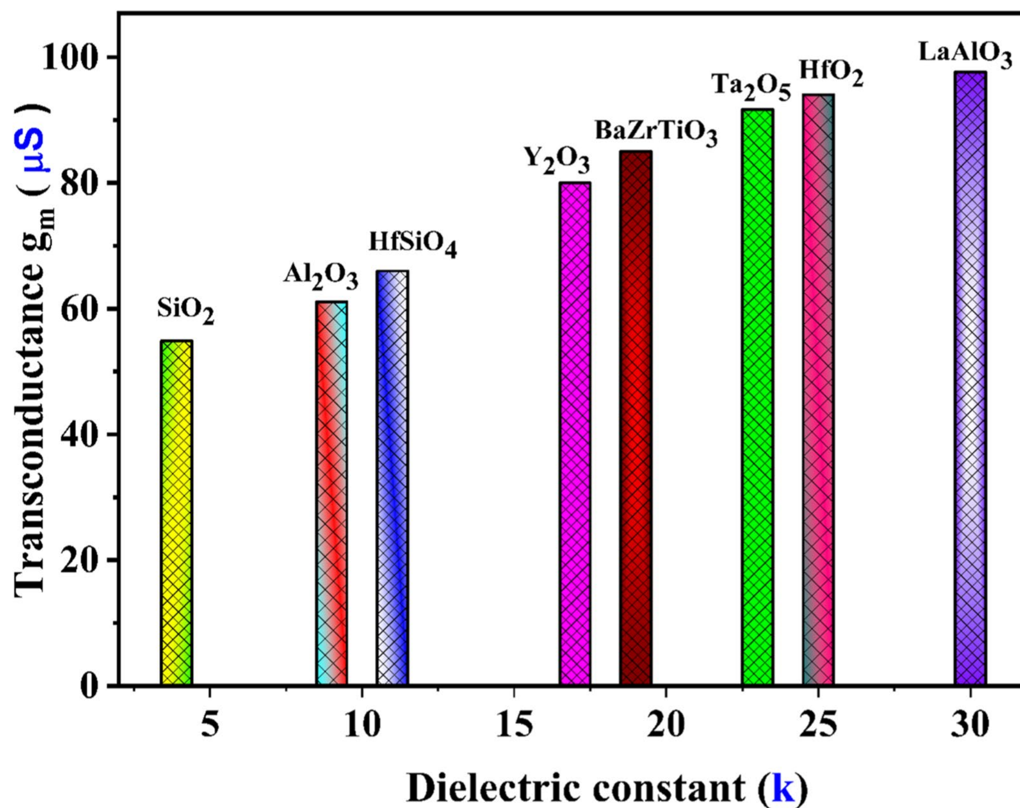

Fig. 13 The transconductance, g_m , at V_{DS} = 0.4 V and V_{GS} = 0.7 V versus the dielectric constant k.

to its high dielectric constant (~ 30), larger band offset with graphene, and robust breakdown characteristics.[63,64] Experimentally, graphene FETs with $LaAlO_3$ demonstrate higher ON/Off ratios, improved subthreshold swing, and enhanced thermal stability compared to devices using HfO_2 or Al_2O_3.[63,65]

$LaAlO_3$ enabling ultrathin equivalent oxide thickness (EOT) down to 0.31 nm without forming an interfacial SiO_2 layer, which commonly occurs with HfO_2 and Al_2O_3. This direct $LaAlO_3$/Si interface results in significantly lower interface trap densities and improved thermal stability, as we mentioned before, by suppressing interfacial layer growth that degrades device performance. Leakage current measurements show that $LaAlO_3$ gate stacks achieve leakage currents at least one order of magnitude lower than Hf-based dielectrics at similar EOTs, and up to six orders of magnitude lower than SiO_2, due to larger conduction and valence band offsets ($\Delta E_c \approx 1.9$ eV, $\Delta E_v \approx$ 2.2 eV) that reduce carrier tunneling. $LaAlO_3$ also exhibits robust thermal stability, allowing low-temperature fabrication compatible with advanced device architectures without degrading the dielectric properties. In contrast, HfO_2 and Al_2O_3 often require additional passivation layers to control interface traps and suffer from higher leakage and less stable effective work functions under thermal annealing. $LaAlO_3$ stable effective work function and tunable threshold voltage through La/(La + Al) ratio adjustment further enhance device design flexibility. Overall, $LaAlO_3$ offers quantitatively superior interface quality, lower leakage, higher dielectric constant, and better thermal stability than HfO_2 and Al_2O_3, making it the optimal high-k dielectric for high-performance, scaled CMOS devices.[66–73] Theoretical studies further confirm that $LaAlO_3$ preserves graphene's linear Dirac cone dispersion with minimal perturbation, unlike some other dielectrics that may induce bandgap opening or Fermi-level pinning, which degrade device performance.[74] These combined advantages make $LaAlO_3$ the preferred dielectric for our study. The incorporation of lanthanum aluminate ($LaAlO_3$) as the gate dielectric material in the GNRFET leads to improved transconductance, yielding a value of 88.5 μS. In contrast, when silicon dioxide (SiO_2) is employed as the gate dielectric, the transconductance drops to 55 μS. Various dielectric materials were used for comparison with lanthanum aluminate, this comparison underscoring the significant role that the choice of dielectric material plays in optimizing the performance of GNRFETs, particularly in improving their transconductive properties. A higher dielectric constant leads to a larger gate capacitance, which in turn results in a higher transconductance. This

increased transconductance means a larger change in drain current for a given change in gate voltage, improving the sensor's sensitivity to changes in the channel conductance induced by gas adsorption.[75,76] All parameters examined in this study have been selected with careful consideration, owing to their significant influence on the characteristics of GNRFET gas sensors

Practical Feasibility and Experimental Validation and Benchmarking of *I–V* Characteristics

While the present study focuses on theoretical modeling and simulation, it is important to consider the practical feasibility of fabricating the proposed GNRFET structures. Recent advances in nanofabrication have demonstrated the viability of constructing GNRFETs with channel lengths below 20 nm and integrating high-κ dielectrics such as $LaAlO_3$ [79, 80, 81] . Techniques including bottom–up synthesis, transfer-free integration, and advanced lithography have enabled the production of GNRFETs with excellent electrical characteristics and scalability[78,, 80]).

For example, Wang et al.[73] reported the fabrication of all-semiconducting sub-10-nm GNRFETs with high ON/OFF ratios and robust performance at room temperature. Similarly, Cai et al.[78] and Kolmer et al.[79] achieved atomically precise GNRs and demonstrated their integration into device architectures compatible with large-scale production. These experimental achievements closely align with the device parameters and performance metrics predicted in our theoretical analysis. The successful implementation of high-κ dielectrics, including $LaAlO_3$, further supports the practical relevance and scalability of our proposed sensor design [81, 82]). Thus, our findings are not only theoretically robust but also experimentally attainable, paving the way for future development of high-performance GNRFET-based sensors.

To validate the accuracy and reliability of our GNRFET gas sensor model, particularly its current voltage (*I–V*) characteristics, we benchmarked our simulation results against existing empirical data and advanced simulation studies reported in the literature.

Mahmoudi et al.[51] presented detailed simulations of GNRFET gas sensors exposed to ammonia, analyzing the output *I–V* characteristics using a model that incorporated the Poisson equation and quantum transport effects. Their results showed a sensitivity of approximately 2.7% at 1 ppm NH_3 concentration, with clear modulation of the drain current upon gas exposure.

Our simulations demonstrate similar trends, including shifts in the *I–V* curves corresponding to varying ammonia concentrations, confirming the model capability to capture the essential sensing physics.

Further, a study by Kheirabadi et al.[83] experimentally investigated bilayer armchair GNRs and reported selective gas-sensing behavior, where changes in conductance were linked to gas adsorption. Although their focus was on different gases, the observed modulation of electronic transport aligns qualitatively with our *I–V* characteristic shifts under ammonia exposure.

Moreover, the work by Rashid et al.[21] simulated GNRFET devices under varying gate voltages and gas molecule adsorption, showing that the presence of target gases significantly alters the *I–V* curves due to charge transfer effects. This supports our approach of modeling the gate voltage dependence of current modulation, which enhances the sensor selectivity and sensitivity.

Importantly, the double-gate GNRFET architecture simulated by Tamersit et al.[75] using the nonequilibrium Green function formalism demonstrated that operating the sensor in the subthreshold regime maximizes the sensitivity, with pronounced changes in *I–V* characteristics upon gas adsorption. Our model similarly predicts enhanced sensitivity and sharper *I–V* modulation in this regime, validating the choice of device architecture and operating conditions.

On the experimental front, vertical graphene FETs reported by Song et al.[84] exhibited significant *I–V* modulation upon ammonia exposure, with detection limits as low as 86 ppb and ON/OFF current ratios up to 10^3. While device structures differ, the underlying mechanism of current modulation by adsorbed gas molecules parallels our GNRFET model, reinforcing its practical relevance.

Collectively, these empirical and simulation benchmarks confirm that our GNRFET gas sensor model accurately reproduces key *I–V* characteristic behaviors observed in state-of-the-art devices. This validation supports the model utility for optimizing sensor design and predicting performance under various gas concentrations and operating conditions.

Conclusions

We have developed a rigorous simulation framework based on a robust analytical model implemented in MATLAB to investigate the current–voltage (*I–V*) characteristics of graphene nanoribbon field-effect transistors (GNRFETs). The results demonstrate a significant modulation of the drain current upon exposure to ammonia (NH_3), with an increase of two orders of magnitude from 10^{-7} A to 10^{-5} A at a concentration of 300 ppm. This pronounced enhancement confirms the high sensitivity of GNRFETs to NH_3 and underscores their potential as effective gas-sensing platforms. These findings provide valuable insights into the charge transfer mechanisms influencing device response and

establish a foundation for the design and optimization of graphene-based gas sensors for environmental and industrial applications.

A systematic analysis was performed to investigate the effects of temperature, gate length, and dual oxide layer thickness on key device performance parameters, and the results indicate a positive correlation between drain current (I_{ds}) and both top-gate oxide thickness and ambient temperature, whereas an inverse relationship was observed with channel length and back-gate oxide thickness. Moreover, the study has highlighted the significant impact of GNR widths (10 nm and 20 nm) on electronic properties, attributable to quantum confinement effects. Utilizing lanthanum aluminate ($LaAlO_3$) as the gate dielectric, critical correlations were established that enhance the understanding of drain current sensitivity, thereby informing the optimization of GNRFETs for gas-sensing applications.

This study provides valuable insights and design guidelines for optimizing GNRFET configurations to enhance gas-sensing performance, thereby reinforcing their applicability in advanced electronic systems. The findings contribute to the broader field of gas sensor technology and lay the groundwork for future developments in sensitive and efficient detection platforms. Understanding the effects of prolonged ammonia (NH_3) exposure and doping on transistor properties is essential for assessing device stability and performance. Future work will focus on investigating the impact of extended NH_3 exposure on the electrical characteristics and reliability of GNRFETs, as well as examining the influence of various doping strategies. Additionally, subsequent studies will address the roles of thermal noise and scattering mechanisms, which are critical factors for optimizing device operation and improving sensor sensitivity. These topics will be explored in detail in forthcoming publications.

Author Contributions The manuscript was written through contributions of all authors. All authors have given approval to the final version of the manuscript.

Funding The authors declare that no funds, grants, or other support were received during the preparation of this manuscript.

Data Availability The data that support the findings of this study are available from the corresponding author upon reasonable request.

Conflict of interest There is no conflict of interest among the contributing authors.

References

1. O.G. Simionescu, A. Avram, B. Adiaconiţă, P. Preda, C. Pârvulescu, F. Năstase, and M. Avram, Field-effect transistors based on single-layer graphene and graphene-derived materials. *Micromachines* 14, 1096 (2023).
2. A.K. Geim and K.S. Novoselov, The rise of graphene. *Nat. Mater.* 6, 183 (2007).
3. J.H. Chen, C. Jang, S. Xiao, M. Ishigami, and M.S. Fuhrer, *Nat. Nanotechnol.* 3, 206 (2008).
4. K.S. Novoselov, A.K. Geim, S.V. Morozov, D.E. Jiang, Y. Zhang, S.V. Dubonos, I.V. Grigorieva, and A.A. Firsov, Electric field effect in atomically thin carbon films. *Science* 306, 666–669 (2004).
5. A.H. Castro Neto, F. Guinea, N.M.R. Peres, K.S. Novoselov, and A.K. Geim, The electronic properties of graphene. *Rev. Mod. Phys.* 81, 109–162 (2009).
6. Y. Xu, Z. Li, and W. Duan, Thermal and thermoelectric properties of graphene. *Small* 10, 2182 (2014).
7. M. Sang, J. Shin, K. Kim, and K.J. Yu, Electronic and thermal properties of graphene and recent advances in graphene-based electronics applications. *Nanomaterials* 9, 374 (2019).
8. F. Schwierz, Graphene transistors. *Nat. Nanotechnol.* 5, 487–496 (2010).
9. Y.W. Son, M.L. Cohen, and S.G. Louie, Energy gaps in graphene nanoribbons. *Phys. Rev. Lett.* 97(21), 216803 (2006).
10. M.Y. Han, B. Özyilmaz, Y. Zhang, and P. Kim, Energy band-gap engineering of graphene nanoribbons. *Phys. Rev. Lett.* 98(20), 206805 (2007).
11. L.A. Openov and A.I. Podlivaev, Insulator band gap in graphane nanoribbons. *Semiconductors* 45, 633 (2011).
12. M. Ghadiry, R. Ismail, M. Saeidmanesh, M. Khaledian, and A.A. Manaf, Graphene nanoribbon field-effect transistor at high bias. *Nanoscale Res. Lett.* 9, 1–5 (2014).
13. H. Owlia and P. Keshavarzi, Investigation of the novel attributes of a double-gate graphene nanoribbon FET with AlN high-κ dielectrics. *Superlattices Microstruct.* 75, 613 (2014).
14. M.R. Moslemi, M.H. Sheikhi, K. Saghafi, and M.K. Moravvej-Farshi, Electronic properties of a dual-gated GNR-FET under uniaxial tensile strain. *Microelectron. Reliab.* 52, 2579 (2012).
15. M.A. Eshkalak, Graphene nano-ribbon field effect transistor under different ambient temperatures. *Iran. J. Electr. Electron. Eng.* 12, 147 (2016).
16. Y. Sun et al., Advances in two-dimensional layered materials for gas sensing. *Sens. Actuators B Chem.* 394, 133100 (2024).
17. J. Zhang et al., Recent advances in chemoresistive gas sensors using two-dimensional materials. *Sensors* 24, 1 (2024).
18. L. Chen et al., Recent advances in 2D MXene-based heterostructures for gas sensing. *Nanoscale* (2025).
19. J.K. Ko, I.H. Park, K. Hong, and K.C. Kwon, Recent advances in chemoresistive gas sensors using two-dimensional materials. *Nanomaterials* 14, 1397 (2024).
20. Y. Xie, Z. Zhang, F. Meng, S. Huo, X. Hu, P. Niu, and E. Wu, Strategies and challenges for improving the performance of two-dimensional materials-based gas sensors. *Adv. Phys. X* 9, 2288353 (2024).
21. M.H. Rashid, A. Koel, and T. Rang, Simulations of graphene nanoribbon field effect transistor for the detection of propane and butane gases: a first principles study. *Nanomaterials* 10, 98 (2020).
22. E. Morales-Narváez, and A. Merkoçi, Graphene oxide as an optical biosensing platform. *Adv. Mater.* 24, 3298 (2012).
23. S.S. Varghese, S. Lonkar, K.K. Singh, S. Swaminathan, and A. Abdala, Recent advances in graphene-based gas sensors. *Sens. Actuators B Chem.* 218, 160–183 (2015).
24. W. Yuan and G. Shi, Graphene-based gas sensors. *J. Mater. Chem. A* 1, 10078 (2013).
25. Y. Zhang, J. Zhang, Y. Jiang, Z. Duan, B. Liu, Q. Zhao, and H. Tai, Ultrasensitive flexible NH_3 gas sensor based on polyaniline/

$SrGe_4O_9$ nanocomposite with ppt-level detection ability at room temperature. *Sens. Actuators B Chem.* 319, 128293 (2020).
26. R.S. Andre, F.M. Shimizu, C.M. Miyazaki, A. Riul Jr., D. Manzani, S.J. Ribeiro, and D.S. Correa, Hybrid layer-by-layer (LbL) films of polyaniline, graphene oxide and zinc oxide to detect ammonia. *Sens. Actuators B Chem.* 238, 795 (2017).
27. D. Zhang, J. Liu, C. Jiang, A. Liu, and B. Xia, Quantitative detection of formaldehyde and ammonia gas via metal oxide-modified graphene-based sensor array combining with neural network model. *Sens. Actuators B Chem.* 240, 55–65 (2017).
28. H.J. Yoon, J.H. Yang, Z. Zhou, S.S. Yang, and M.M.C. Cheng, Carbon dioxide gas sensor using a graphene sheet. *Sens. Actuators B Chem.* 157, 310 (2011).
29. G. Ko, H.Y. Kim, J. Ahn, Y.M. Park, K.Y. Lee, and J. Kim, Graphene-based nitrogen dioxide gas sensors. *Curr. Appl. Phys.* 10, 1002 (2010).
30. X. Lin, J. Ni, and C. Fang, Adsorption capacity of H_2O, NH_3, CO, and NO_2 on the pristine graphene. *J. Appl. Phys.* (2013). https://doi.org/10.1063/1.4776239.
31. N. Joshi, T. Hayasaka, Y. Liu, H. Liu, O.N. Oliveira, and L. Lin, A review on chemiresistive room temperature gas sensors based on metal oxide nanostructures, graphene and 2D transition metal dichalcogenides. *Microchim. Acta* 185, 1 (2018).
32. R. Mahmood, Numerical analysis of switching and current-voltage characteristics of graphene nano-ribbon field effect transistors. *Am. J. Eng. Res.* 5, 23 (2016).
33. A. Wasfi, A. Al Hamarna, O.M.H. Al Shehhi, H.F.M. Al Ameri, and F. Awwad, Graphene nanoribbon field effect transistor simulations for the detection of sugar molecules: semi-empirical modeling. *Sensors* 23, 3010 (2023).
34. T. Radsar, H. Khalesi, and V. Ghods, Improving the performance of graphene nanoribbon field-effect transistors by using lanthanum aluminate as the gate dielectric. *J. Comput. Electron.* 19, 1507 (2020).
35. K. Tamersit, An ultra-sensitive gas nanosensor based on asymmetric dual-gate graphene nanoribbon field-effect transistor: proposal and investigation. *J. Comput. Electron.* 18, 846 (2019).
36. V. Ryzhii, M. Ryzhii, A. Satou, and T. Otsuji, Current-voltage characteristics of a graphene-nanoribbon field-effect transistor. *J. Appl. Phys.* (2008). https://doi.org/10.1063/1.2917284.
37. E. Akbari, Z. Buntat, M.H. Ahmad, A. Enzevaee, R. Yousof, S.M.Z. Iqbal, and H. Karimi, Analytical calculation of sensing parameters on carbon nanotube based gas sensors. *Sensors* 14, 5502 (2014).
38. W.S. Hwang, P. Zhao, K. Tahy, L.O. Nyakiti, V.D. Wheeler, R.L. Myers-Ward et al., Graphene nanoribbon field-effect transistors on wafer-scale epitaxial graphene on SiC substrates. *APL Mater.* 3, 011101 (2015).
39. L. Brey and H.A. Fertig, Electronic states of graphene nanoribbons studied with the Dirac equation. *Phys. Rev. B* 73, 235411 (2006).
40. S. Datta, *Quantum Transport: Atom to Transistor* (Cambridge: Cambridge University Press, 2005).
41. G. Fiori and G. Iannaccone, On the possibility of tunable bandgap in graphene nanoribbons. *IEEE Electron Device Lett.* 28, 760–762 (2007).
42. M. Luisier and G. Klimeck, Atomistic full-band simulations of silicon nanowire transistors: effects of electron-phonon scattering. *Phys. Rev. B* 80, 155430 (2009).
43. Z. Johari, M.T. Ahmadi, D.C.Y. Chek, N.A. Amin, and R. Ismail, Modelling of graphene nanoribbon Fermi energy. *J. Nanomater.* 2010, 909347 (2010).
44. V. Kažukauskas, V. Kalendra, C.W. Bumby, B.M. Ludbrook, and A.B. Kaiser, Electrical conductivity of carbon nanotubes and polystyrene composites. *Phys. Status Solidi C* 5, 3172–3174 (2008).
45. E. Akbari, V.K. Arora, A. Enzevaee, M.T. Ahmadi, M. Saeidmanesh, M. Khaledian et al., An analytical approach to evaluate the performance of graphene and carbon nanotubes for NH_3 gas sensor applications. *Beilstein J. Nanotechnol.* 5, 726–734 (2014).
46. R. Marani and A.G. Perri, Semi-empirical modeling of CNTFETs including temperature-dependent bandgap effects. *J. Comput. Electron.* 16, 564–572 (2017).
47. D. Gunlycke, D.A. Areshkin, and C.T. White, Semiconducting graphene nanostrips with edge disorder. *Appl. Phys. Lett.* 90, 143112 (2007).
48. A. Hosseingholipourasl, S. Hafizah Syed Ariffin, Y.D. Al-Otaibi, E. Akbari, F.K. Hamid, S.S.R. Koloor, and M. Petrů, Analytical approach to study sensing properties of graphene based gas sensor. *Sensors* 20, 1506 (2020).
49. B. Cho, J. Yoon, M.G. Hahm, D.H. Kim, A.R. Kim, Y.H. Kahng, S.-W. Park, Y.-J. Lee, S.-G. Park, J.-D. Kwon, C.S. Kim, M. Song, Y. Jeong, K.-S. Nam, and H.C. Ko, Graphene-based gas sensor: metal decoration effect and application to a flexible device. *J. Mater. Chem. C* 2, 5280–5285 (2014).
50. K. Tamersit and D. Fayçal, Nuclear instruments and methods in physics research section a: accelerators. *Spectrom. Detect. Assoc. Equip.* 901, 32 (2018).
51. A. Mahmoudi, M. Troudi, Y. Bergaoui, P. Bondavalli, and N. Sghaier, Analysis of simulated output characteristics of gas sensor based on graphene nanoribbon. *J. Nanomater.* 2016, 9835340 (2016).
52. A. Misra, Carbon nanotubes and graphene-based chemical sensors. *Curr. Sci.* 106, 419–429 (2014).
53. K.R. Amin and A. Bid, Graphene as a sensor. *Curr. Sci.* 106, 430–436 (2014).
54. A. Singh, M.A. Uddin, T. Sudarshan, and G. Koley, Tunable reverse-biased graphene/silicon heterojunction schottky diode sensor. *Small* 10, 1555–1565 (2014).
55. S. Kim, G. Lee, and J. Kim, *ECS J. Solid State Sci. Technol.* 7, 3065 (2018).
56. S. Lone, A. Bhardwaj, A.K. Pandit, S. Gupta, and S. Mahajan, A review of graphene nanoribbon field-effect transistor structures. *J. Electron. Mater.* 50, 3169–3186 (2021).
57. Z. Zhang, X. Zhang, W. Luo, H. Yang, Y. He, Liu, Y.X. Zhang, and G. Peng, *Nanoscale Res. Lett.* 10, 1–8 (2015).
58. M. Shooshtari, Ammonia gas sensors based on multi-wall carbon nanofiber field effect transistors by using gate modulation. *Colloids Surf A Physicochem Eng Asp* 704, 135563 (2025).
59. R. Djamil, K. Aicha, A. Cherifa, and F. Djeffal, Impacts of high-k gate dielectrics and low temperature on the performance of nanoscale CNTFETs. *J. Comput. Electron.* 15, 1308–1315 (2016).
60. M. Freitag, M. Steiner, Y. Martin, V. Perebeinos, Z. Chen, J.C. Tsang, and P. Avouris, Energy dissipation in graphene field-effect transistors. *Nano Lett.* 9, 1883–1888 (2009).
61. G. Venugopal and S.J. Kim, Temperature dependent transfer characteristics of graphene field effect transistors fabricated using photolithography. *Curr. Appl. Phys.* 11, S381–S384 (2011).
62. D.B. Farmer, R. Golizadeh-Mojarad, V. Perebeinos et al., Chemical doping and electron-hole conduction asymmetry in graphene devices. *Nano Lett.* 9, 388–392 (2009).
63. N. Shukla, A. Kumar, M. Kumar et al., $LaAlO_3$ as a high-k gate dielectric for graphene field-effect transistors: fabrication and characterization. *ACS Appl. Mater. Interfaces* 7, 11051–11058 (2015).
64. O. Kwon, J. Lee, S. Kim et al., Low leakage and high reliability of $LaAlO_3$ gate dielectric on graphene for high-performance devices. *Adv. Electron. Mater.* 4, 1700452 (2018).
65. S.J. Chae, H. Kim, Y. Lee et al., Enhanced performance of graphene field-effect transistors with $LaAlO_3$ gate dielectric. *IEEE Electron Device Lett.* 38, 628–631 (2017).

66. J. Robertson, High dielectric constant oxides. *Eur. Phys. J. Appl. Phys.* 28, 265–291 (2004).
67. J.P. Chang, M.A. Alam, and S. Guha, $LaAlO_3$ gate dielectric for CMOS applications. *Microelectron. Eng.* 84, 2096–2100 (2007).
68. B. Lu, T. Zhang, and H. Wang, Comparison of HfAlO, HfO_2/Al_2O_3, and HfO_2 on n-type GaAs using atomic layer deposition. *Appl. Surf. Sci.* 387, 1035–1040 (2016). https://doi.org/10.1016/j.apsusc.2016.07.164.
69. J.J. Gu, X. Wang, Y.Q. Wu, R.G. Gordon, and P.D. Ye, Variability improvement by interface passivation and EOT scaling of InGaAs nanowire MOSFETs with $LaAlO_3$-based gate stack. *IEEE Electron Device Lett.* 34, 491–493 (2013).
70. M. Houssa, E. Simoen, and C. Claeys, Band offsets and leakage currents in $LaAlO_3$-based gate stacks. *Appl. Phys. Lett.* 89, 222903 (2006).
71. J.J. Gu, Y.Q. Liu, M. Xu, Y.Q. Wu, R.G. Gordon, and P.D. Ye, High performance atomic-layer-deposited $LaLuO_3$/Ge-on-insulator p-channel MOSFET with thermally grown GeO_2 as interfacial passivation layer. *Appl. Phys. Lett.* 97, 121062 (2010).
72. X. Wang, H. Huang, and Y. Zhang, Comparative study of Al_2O_3 and HfO_2 for surface passivation of semiconductor devices. *Phys. Status Solidi A* 218, 2100073 (2021).
73. J.P. Chang, M.A. Alam, and S. Guha, Tunable threshold voltage and stable effective work function of $LaAlO_3$ gate dielectrics. *Microelectron. Eng.* 86, 1636–1639 (2009).
74. K.H. Jin, J.H. Park, and J.K. Kim, First-principles study of $LaAlO_3$/graphene interface: electronic structure and band alignment. *Phys. Rev. B* 86, 045445 (2012).
75. K. Tamersit, F. Djeffal, and M. Meguellati, Numerical modeling of a deep submicron gas sensor based on double-gate graphene nanoribbon field-effect transistor. *Proc. World Congr. Eng.* 1, 396–399 (2015).
76. X. Tang, M. Debliquy, D. Lahem, Y. Yan, and J.P. Raskin, A review on functionalized graphene sensors for detection of ammonia. *Sensors.* 21(4), 1443 (2021).
77. X. Wang et al., Room-temperature all-semiconducting sub-10-nm graphene nanoribbon field-effect transistors. *Science* 324, 768–771 (2009).
78. J. Cai et al., Atomically precise bottom-up fabrication of graphene nanoribbons. *Nature* 466, 470–473 (2010).
79. M. Kolmer et al., Electronic structure of atomically precise graphene nanoribbons. *Science* 369, 571–575 (2020).
80. P.B. Bennett et al., Etchant-free transfer of wafer-scale monolayer graphene grown by chemical vapor deposition. *Nanoscale* 6, 11818–11824 (2014).
81. C.H. Ahn, J.-M. Triscone, and J. Mannhart, Electric field effect in correlated oxide systems. *Nature* 424, 1015–1018 (2003).
82. G.F. Dionne, *High Dielectric Constant Materials: VLSI MOSFET Applications* (Berlin: Springer, 2006).
83. S.J. Kheirabadi, R. Ghayour, M. Sanaee, and B. Jooj, Selective gas sensor based on bilayer armchair graphene nanoribbon. *Phys. E* 129, 114635 (2021).
84. H. Song, J. Liu, H. Lu, C. Chen, and L. Ba, High sensitive gas sensor based on vertical graphene field effect transistor. *Nanotechnology* 31, 165503 (2020).
85. N.S. Struchkov, A.V. Romashkin, M.K. Rabchinskii, S.D. Saveliev, P.D. Cherviakova, R.G. Chumakov, and A.V. Emelianov, Aminated reduced graphene oxide-carbon nanotube composite gas sensors for ammonia recognition. *Sens. Actuators B Chem.* 417, 136088 (2024).

Publisher's Note Springer Nature remains neutral with regard to jurisdictional claims in published maps and institutional affiliations.

Springer Nature or its licensor (e.g. a society or other partner) holds exclusive rights to this article under a publishing agreement with the author(s) or other rightsholder(s); author self-archiving of the accepted manuscript version of this article is solely governed by the terms of such publishing agreement and applicable law.